Interannual variability of the South China Sea associated with El Niño

Chunzai Wang,[1] Weiqiang Wang,[2] Dongxiao Wang,[2] and Qi Wang[3]

Received 30 September 2005; revised 23 November 2005; accepted 30 December 2005; published 30 March 2006.

[1] Interannual sea surface temperature (SST) anomalies in the South China Sea (SCS) are largely influenced by El Niño through El Niño–driven atmospheric and oceanic changes. This paper discovers a new observed feature of the SCS SST anomalies: a double-peak evolution following an El Niño event. The first and second peaks occur around February and August, respectively, in the subsequent year of the El Niño year (denoted by February [+1] and August [+1]). During and after the mature phase of El Niño, a change of atmospheric circulation alters the local SCS near-surface air temperature, humidity, cloudiness, and monsoon wind. These factors influence surface heat fluxes and oceanic flows over the SCS that can either warm or cool the SCS depending upon stages of SST anomaly evolution. The shortwave radiation and latent heat flux anomalies are major contributions to the first peak of the SCS SST anomalies, although the geostrophic heat advections warm the western boundary region of the SCS. After the first peak of February [+1], both the Ekman and geostrophic heat advections, assisted with a reduction of the net heat flux anomalies, cool the SCS SST anomalies. In August [+1], the mean meridional geostrophic heat advection makes the SCS SST anomalies peak again. Then, the latent heat flux anomalies (mainly attributed to anomalous air-sea difference in specific humidity) and the mean zonal geostrophic heat advection take over for the cooling of the SCS after the second peak.

Citation: Wang, C., W. Wang, D. Wang, and Q. Wang (2006), Interannual variability of the South China Sea associated with El Niño, *J. Geophys. Res.*, *111*, C03023, doi:10.1029/2005JC003333.

1. Introduction

[2] The largest source of Earth's climate variability in the instrumental record is El Niño–Southern Oscillation (ENSO). Although ENSO's maximum sea surface temperature (SST) anomalies occur in the equatorial eastern and central Pacific, ENSO affects the global ocean. The global nature of ENSO is shown in Figure 1, which displays the correlation between the Nino3 SST anomalies during November–December–January and global SST anomalies during the following February–March–April. These seasons are chosen because ENSO peaks during the boreal winter while its influence on other ocean basins normally peaks 1–2 seasons later [e.g., *Alexander et al.*, 2002]. Figure 1 shows that outside the tropical Pacific significant ENSO-related SST anomalies are found over many places, such as in the tropical North Atlantic, the tropical Indian Ocean, the extratropical North and South Pacific, and the South China Sea.

[3] The influence of ENSO on other tropical oceans is transmitted through the "atmospheric bridges" of atmospheric circulation changes. Using satellite and ship observations and the NCEP-NCAR reanalysis fields, *Klein et al.* [1999] and *Wang* [2002, 2005] suggest and show that the Walker and Hadley circulations can serve as an atmospheric bridge. During the warm phase (El Niño) of ENSO, convective activity in the equatorial western Pacific shifts eastward. This shift in convection leads to an altered Walker circulation, with anomalous ascent over the equatorial central and eastern Pacific, and anomalous descent over the equatorial Atlantic and the equatorial Indo-western Pacific region. Thus the Hadley circulation strengthens over the eastern Pacific but weakens over the Atlantic and Indo-western Pacific sectors. These anomalous Walker and Hadley circulations result in variations in surface wind, air temperature, humidity, and cloud cover that in turn influence surface heat fluxes and ocean circulations over other ocean basins and then change SST.

[4] The correlation map of Figure 1 shows that the South China Sea (SCS) is largely influenced by ENSO. The time series of the SCS and Nino3 SST anomalies in all calendar months from 1950 to 2002 are compared in Figure 2. Every ENSO event is associated with a change in the SCS SST anomalies. The calculation shows that maximum correlation of 0.51 occurs when the Nino3 SST anomalies lead the SCS SST anomalies by 5 months [also see *Klein et al.*, 1999; *Wang et al.*, 2000]. In spite of a strong ENSO impact on the

[1] Atlantic Oceanographic and Meteorological Laboratory, Physical Oceanography Division, NOAA, Miami, Florida, USA.
[2] Key Laboratory of Tropical Marine Environmental Dynamics, South China Sea Institute of Oceanology, Chinese Academy of Sciences, Guangzhou, China.
[3] Department of Meteorology, Physical Oceanography Laboratory, Ocean University of China, Qingdao, China.

0148-0227/06/2005JC003333$09.00

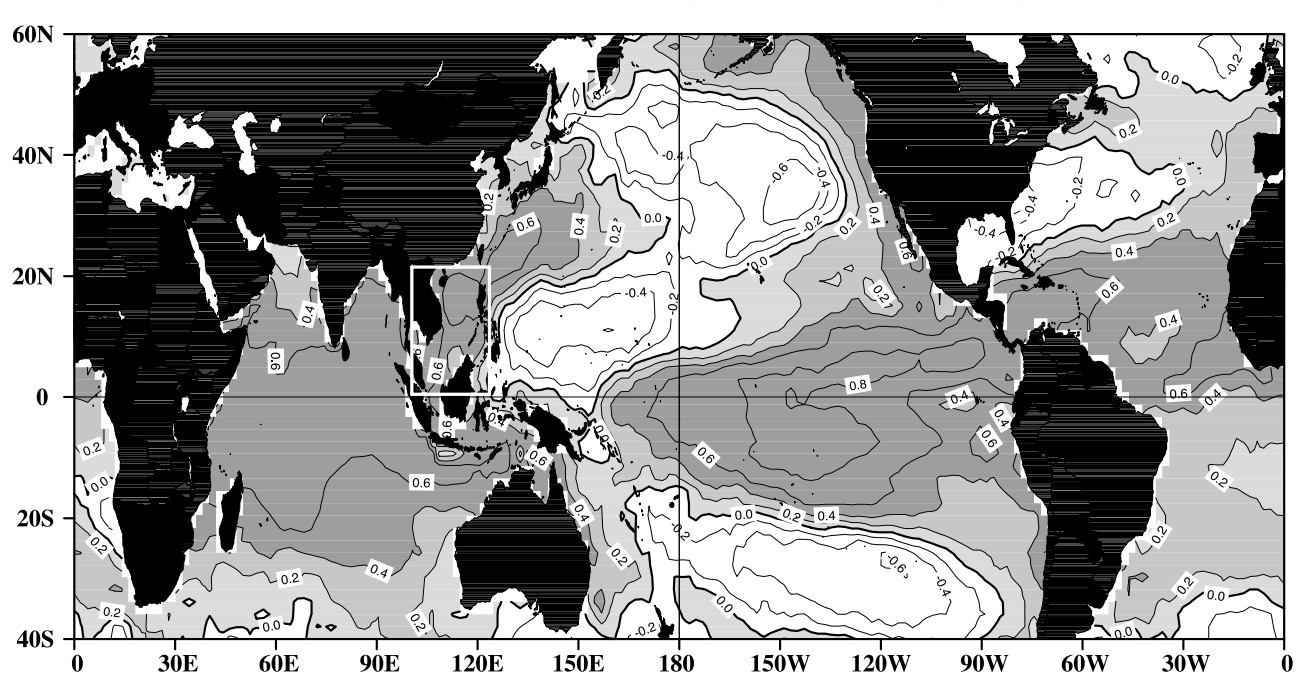

Figure 1. Correlation between the Nino3 (5°S–5°N, 150°W–90°W) SST anomalies during November–December–January (NDJ) and global SST anomalies during the following February–March–April (FMA). The white box represents the region of the South China Sea. The figure is modified from *Wang et al.* [2004].

SCS [e.g., *D. Wang et al.*, 2002; *Q. Wang et al.*, 2002; *Xie et al.*, 2003; *Qu et al.*, 2004; *Liu et al.*, 2004], our understanding of interannual variability in the SCS is very poor. In particular, the mechanisms that are responsible for the SCS interannual SST anomalies are not known. The present paper has two major goals. First, it reports a new observed feature of the SCS SST anomalies: A double-peak evolution in the subsequent year of the El Niño year (the present paper is the first to document this feature). Second, the paper investigates and examines physical processes that generate the SCS interannual SST anomalies.

[5] The rest of the paper is organized as follows. Section 2 describes all data sets used in this paper. Section 3 presents a double-peak feature of the SCS SST anomalies associated with El Niño. Section 4 examines physical processes that generate the SCS SST anomalies over the period of 1950–2002. Section 5 investigates the role of geostrophic heat advections in the SCS SST anomalies during the 1997–1998 El Niño. Finally, Section 6 provides a summary and discussion.

2. Data Sets

[6] Monthly SST, surface wind, and surface heat fluxes of the *da Silva et al.* [1994] data from 1945 to 1993 on a grid of 1° latitude × 1° longitude are used in this study. The da Silva et al. data set is derived primarily from individual observations of comprehensive ocean-atmosphere data set (COADS) [*Woodruff et al.*, 1987]. The data in this data set ends in 1993 and is not updated.

[7] International COADS (ICOADS) is a multinational effort to blend available observations between 1960 and 2002. ICOADS is the world's largest collection of marine surface observations with a nonuniform grid. We use a kriging method with 3° radius to interpolate all data into a grid of 1° latitude × 1° longitude. ICOADS includes many monthly oceanic and atmospheric variables; however, surface heat fluxes include only latent heat flux and sensible heat flux parameter (without transfer coefficients). Therefore we derive or reconstruct the surface heat fluxes in the SCS by using the following bulk formulae for shortwave radiation Q_{SW}, longwave radiation Q_{LW}, latent heat flux Q_{LAT}, and sensible heat flux Q_{SEN}:

$$Q_{SW} = 0.94Q_0(1 - 0.62C + 0.0019\alpha) \quad (1)$$

$$Q_{LW} = \varepsilon\sigma T_a^4\left(0.39 - 0.05e_a^{1/2}\right)\left(1 - bC^2\right) + 4\varepsilon\sigma T_a^3(T_s - T_a) \quad (2)$$

$$Q_{LAT} = \rho_a L C_E U_a(q_s - q_a) \quad (3)$$

$$Q_{SEN} = \rho_a C_P C_E U_a(T_s - T_a), \quad (4)$$

where Q_0 is the clear sky radiance, C is the cloud cover, α is the noon solar altitude, ε = 0.97 is the emissivity of the ocean, $\sigma = 5.67 \times 10^{-8}$ W M^{-2} °K^{-4} is the Stefan-Boltzmann constant, b is the empirical parameter varied with latitude [*Fung et al.*, 1984], ρ_a = 1.15 kg m^{-3} is the air density, $C_E = 1.2 \times 10^{-3}$ is the exchange coefficient, $L = 2.44 \times 10^6$ J kg^{-1} is the latent heat of vaporization, q_s is the

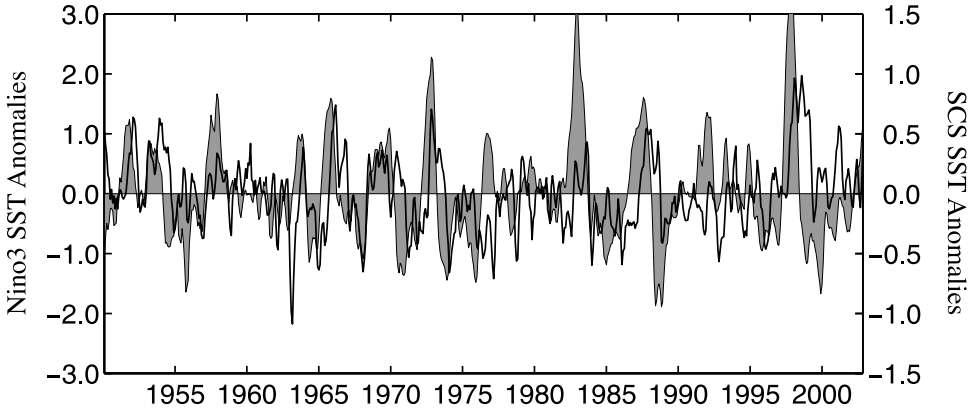

Figure 2. Comparisons of the Nino3 (5°S–5°N, 150°W–90°W) SST anomalies (shaded curve) with the SST anomalies in the South China Sea (SCS; 0.5°N–23.5°N, 100.5°E–123.5°E). The time series are 3-month running means. Maximum correlation of 0.51 occurs when the Nino3 SST anomalies lead the SCS SST anomalies by 5 months.

specific humidity saturated at the sea temperature, q_a is the specific humidity of the air at 10 m elevation, and T_a and T_s are the air and sea temperatures, $U_a = \sqrt{u_a^2 + v_a^2}$ is the wind speed, $C_P = 1.005 \times 10^3$ J kg^{-1} °C^{-1} is the heat capacity, and e_a is the atmospheric vapor pressure.

[8] With the *da Silva et al.* [1994] data set from 1945 to1993 and the reconstructed ICOADS data set from 1960 to 2002 just described, we compare two data sets over the overlapping period and find a good agreement in patterns and temporal variations. We then update the da Silva et al. data set to form a new marine meteorological data set from 1945 to 2002 on a horizontal grid of 1° latitude × 1° longitude over the SCS. In this paper, we will mainly analyze monthly SST, surface wind, and surface heat fluxes.

[9] We also use the Levitus climatological data of the ocean subsurface temperature, salinity, and mixed layer

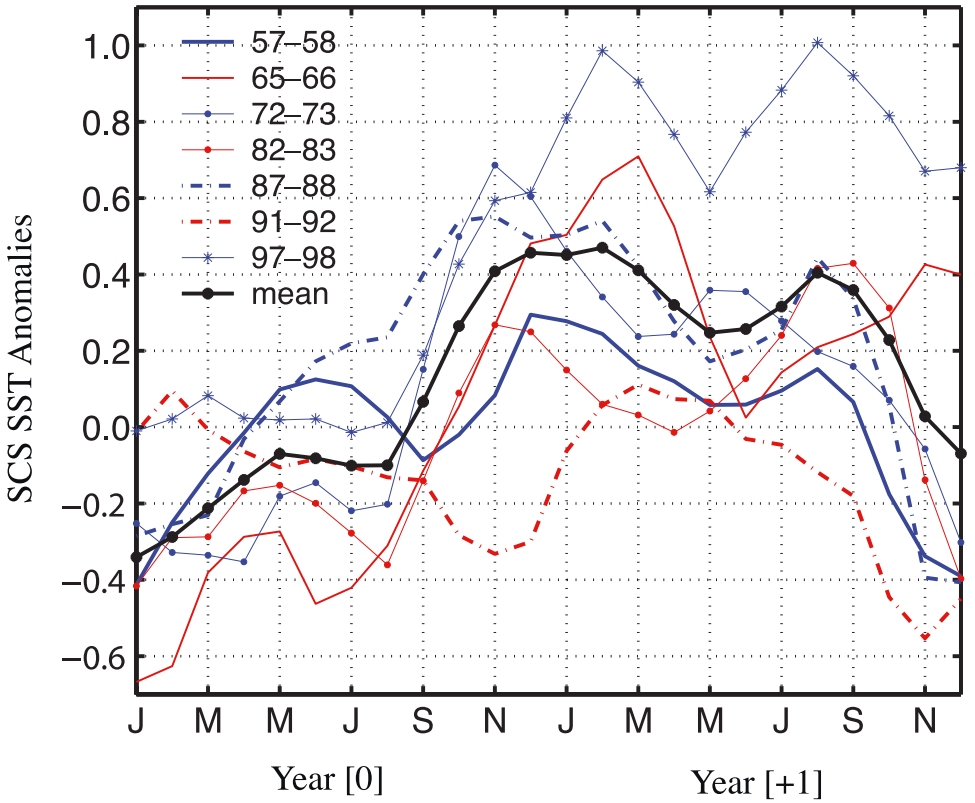

Figure 3. Three-month running means of the South China Sea (SCS) SST anomalies associated with the seven El Niño warm events during the El Niño year (year [0]) and the subsequent year of the El Niño year (year [+1]). The thick black curve represents the mean SST anomalies for six warm events (excluding the 1991–1892 El Niño event).

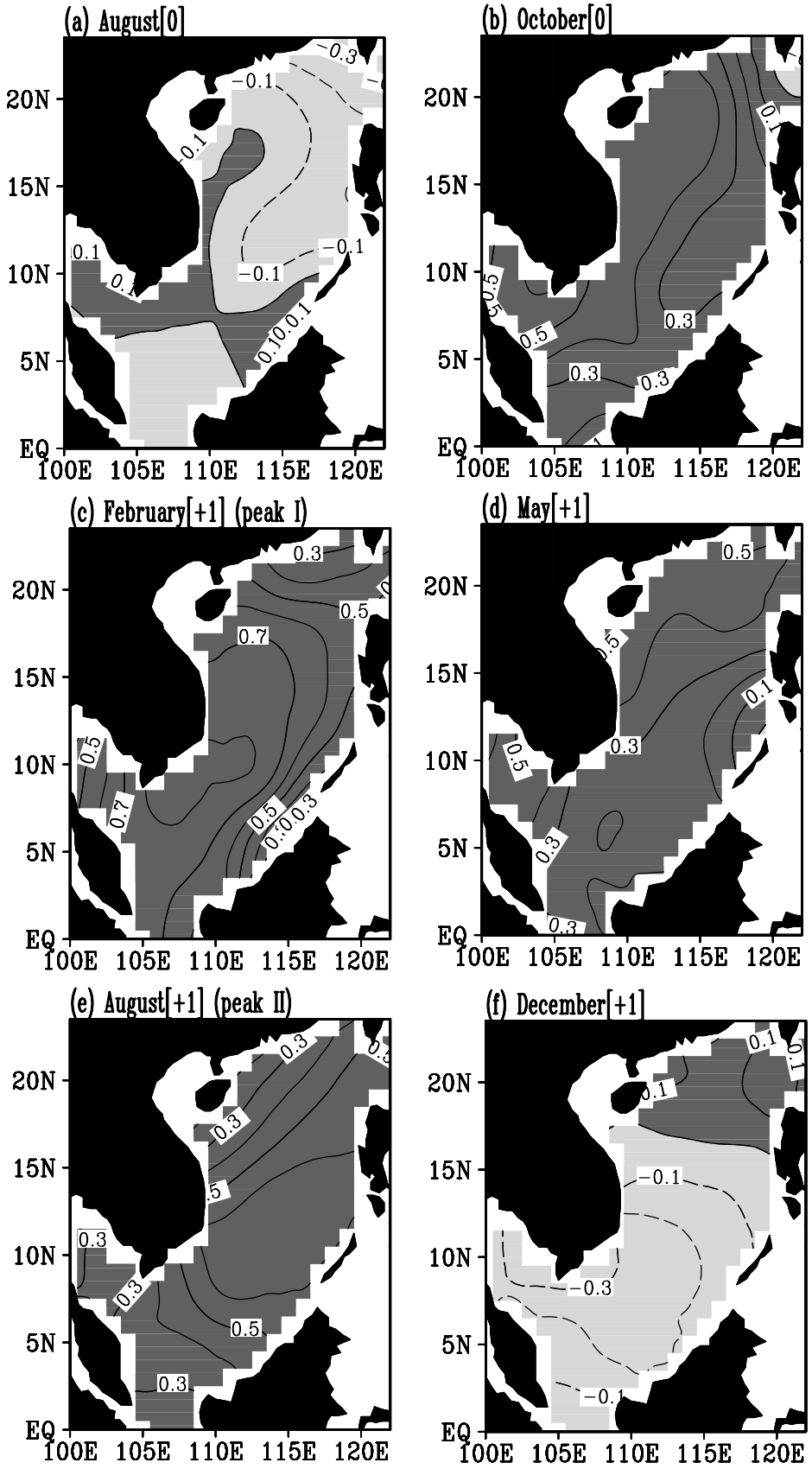

Figure 4. Composites of the South China Sea (SCS) SST anomalies (°C) in (a) August [0], (b) October [0], (c) February [+1], (d) May [+1], (e) August [+1], and (f) December [+1]. [0] and [+1] refer to the El Niño year and the subsequent year of the El Niño year, respectively. Positive (negative) values are given by dark (light) shading and solid (dashed) contour lines.

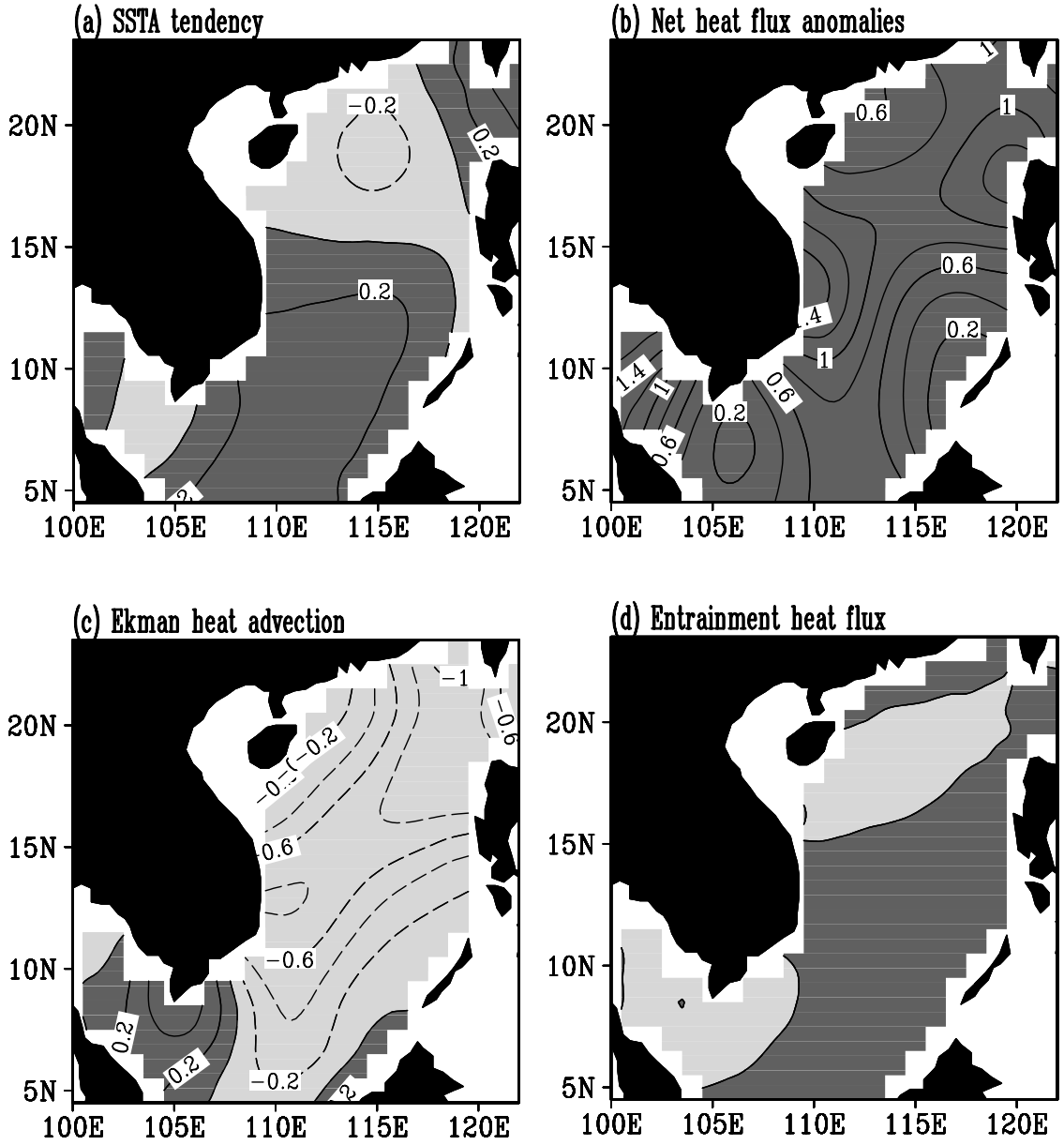

Figure 5. November [0] composites of (a) the SST anomaly tendency, (b) net heat flux anomalies ($Q'_{NET}/\rho C_P \bar{h}$), (c) Ekman heat advections ($-\vec{u}_E \nabla T' - \vec{u}'_E \nabla \bar{T}$), and (d) anomalous entrainment heat flux ($-w'_E \partial \bar{T}/\partial z$) in the SCS. Positive (negative) values are given by dark (light) shading and solid (dashed) contour lines, and contour interval is 0.2°C per 2 months.

depth [*Levitus and Boyer*, 1994]. The Levitus climatology comprises quality controlled ocean profile data averaged onto a global 1° latitude × 1° longitude grid at fixed standard depths.

[10] Finally, the sea surface height (SSH) data set that merges European Remote Sensing (ERS) and TOPEX/Poseidon (T/P) altimetry observations [*Ducet et al.*, 2000] is also utilized. This SSH product is monthly with a grid of 0.25° latitude × 0.25° longitude from 1992 to 2001. The SSH data, assisted with the Levitus climatological data, is used to calculate the geostrophic current in the SCS.

[11] With all of these data sets, we first calculate monthly climatologies on the basis of the full data record period and then anomalies are obtained by subtracting the monthly climatologies from the data. A linear trend removal is applied to the anomaly data at all grid points before our analyses.

3. Double Peak of the SCS SST Anomalies

[12] As stated in the introduction, interannual variability of the SCS is largely influenced by El Niño event. From 1950 to 2002, there are seven significant El Niño warm events: 1957–1958, 1965–1966, 1972–1973, 1982–1983, 1986–1987, 1991–1992, and 1997–1998. Note that we do not consider the two recent and weak El Niños of 2002–2003 and 2004–2005 since our data set records do not cover these two events. The maximum Nino3 SST anomalies for each warm event occur during the calendar months from November to January, except for the 1986–1987 El

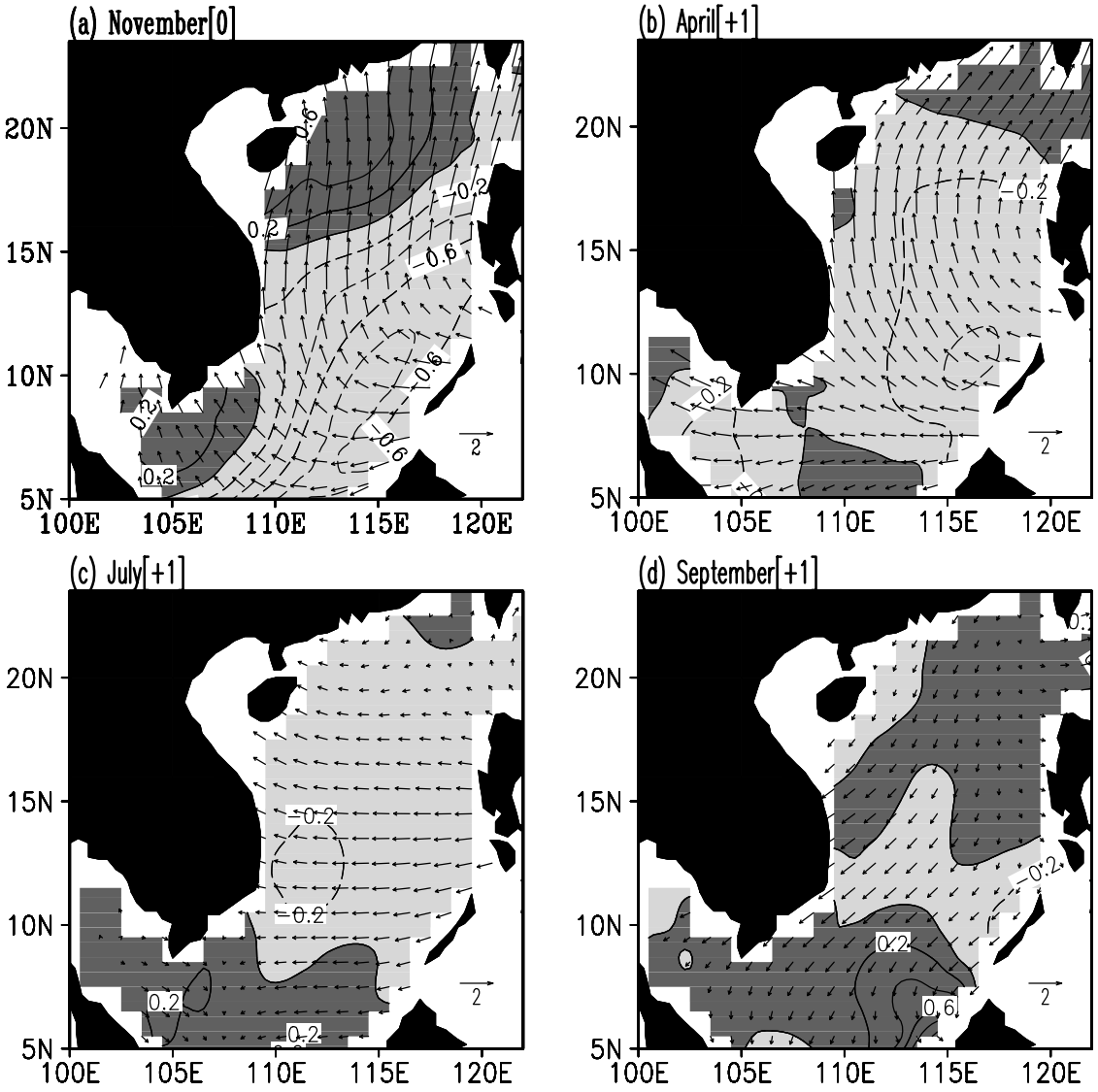

Figure 6. Composites of the wind anomalies (m/s, vectors) and anomalous Ekman pumping velocity $w'_E = curl(\vec{\tau}'/\rho f)$ (10^{-5} m/s, contours and shadings) in (a) November [0], (b) April [+1], (c) July [+1], and (d) September [+1]. Positive (negative) values are given by dark (light) shading and solid (dashed) contour lines.

Niño event which has the largest peak in the following boreal summer (a weak peak in the winter of the El Niño year). Corresponding to these El Niño warm events in the Pacific, the SCS also shows a warm state. Figure 3 displays the SCS SST anomalies associated with the seven El Niño warm events during the El Niño year and the subsequent year of the El Niño year. For the 1986–1987 El Niño, the SCS is warm in the winter of 1987 and the summer of 1988. Therefore we plot the SCS SST anomalies from 1987 to 1988 in Figure 3 for the case of the 1986–1987 El Niño. The SCS SST anomalies begin to warm up in the boreal fall of the El Niño year and the warm state lasts for more than one year. A prominent feature of the SCS SST anomalies is a double peak following El Niño. For all El Niño events except the weak 1991–1992 event, the SCS SST anomalies peak two times during the subsequent year of the El Niño year. In all of the following composite calculations, we will exclude the weak 1991–1992 event. The mean SCS SST anomalies for six warm events (excluding the 1991–1992 event; thick black curve in Figure 3) show that the double peak of the SCS SST anomalies occurs in February [+1] and August [+1], with the average SST anomalies of 0.47°C and 0.41°C, respectively. Note that in this paper, [0] and [+1] refer to the El Niño year and the subsequent year of the El Niño year, respectively.

[13] How the horizontal structure of the SCS SST anomalies evolves can be examined by compositing the SCS SST anomalies during different stages of El Niño, as shown in Figure 4. The SCS is cold in and before August [0] (Figure 4a), and the entire SCS becomes warm in October [0] with maximum positive SST anomalies located in the west half of the basin (Figure 4b). After the basin-scale warming of October [0], the entire SCS remains warm toward the next year of November [+1]. The double peak of the SCS SST anomalies is also evidenced in Figure 4 by

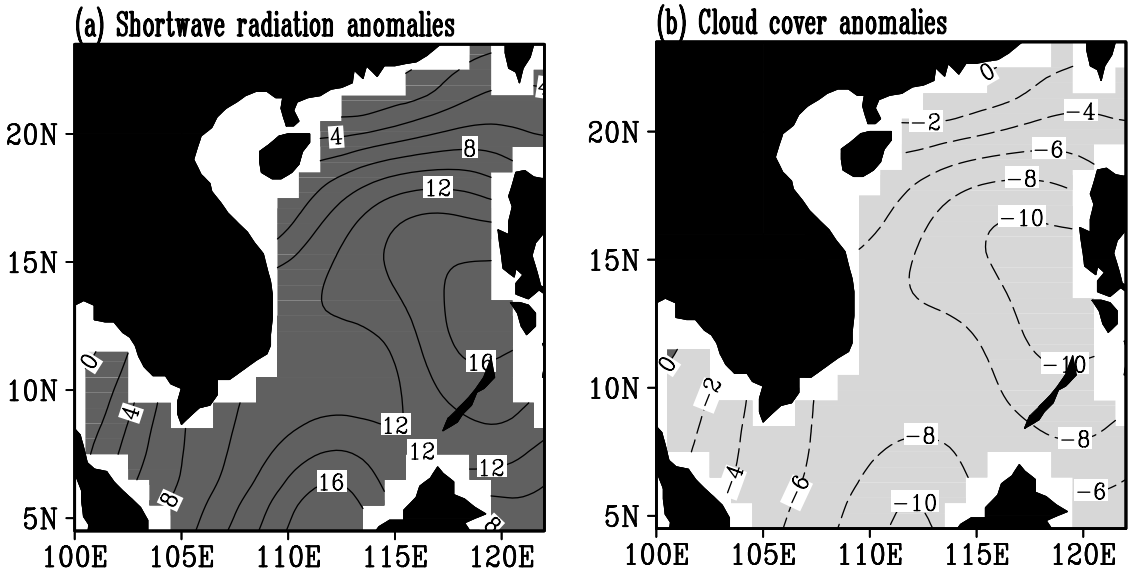

Figure 7. November [0] composites of (a) the shortwave radiation anomalies (W/m^2) and (b) the cloud cover anomalies (%) in the SCS. Positive (negative) values are given by dark (light) shading and solid (dashed) contour lines.

showing that the SCS SST anomalies reach their maximum in February [+1] (Figure 4c), decay toward May [+1] (Figure 4d), and then increase again and peak in August [+1] (Figure 4e). The center of maximum SST anomalies is located in the southern SCS for the first peak (Figure 4c), whereas it is in the central SCS for the second peak (Figure 4e). After the more than one year warming (the entire SCS is still warm in October [+1]), the SCS returns to a cold state in December [+1] (Figure 4f).

4. Processes Generating the SCS SST Anomalies

[14] The focus of this paper is on interannual variability of SST anomalies over the SCS. After linearizing the SST equation, we obtain that

$$\frac{\partial T'}{\partial t} = \frac{Q'_{NET}}{\rho C_P \bar{h}} - \vec{u}_E \cdot \nabla T' - \vec{u}'_E \cdot \nabla \bar{T} - \vec{u}_G \cdot \nabla T' - \vec{u}'_G \cdot \nabla \bar{T} - w'_E \frac{\partial \bar{T}}{\partial z} - \bar{w}_E \frac{\partial T'}{\partial z}, \quad (5)$$

where the overbar denotes the climatological mean and the prime denotes anomaly. T is the SST, Q_{NET} is the net surface heat flux, h is the mixed layer depth, $\vec{u}_E = \left(\vec{\tau} \times \vec{k}\right)/\left(\rho f \bar{h}\right)$ is the Ekman velocity vector, $\vec{u}_G$ is the geostrophic velocity vector, and $w_E = curl(\vec{\tau}/\rho f)$ is the Ekman pumping (entrainment) velocity. The term in the left hand side of equation (5) is the SST anomaly tendency. The terms in the right hand side of equation (5) are the net heat flux anomalies, mean Ekman heat advection, anomalous Ekman heat advection, mean geostrophic heat advection, anomalous geostrophic advection, anomalous entrainment heat flux, and mean entrainment heat flux, respectively. Nonlinear heat advection terms, which are usually small in the SCS, are not considered in this paper.

[15] The Levitus climatological ocean temperature data is used to calculate the mean vertical temperature gradient $\partial \bar{T}/\partial z$. However, we cannot calculate the anomalous vertical temperature gradient $\partial T'/\partial z$ since it requires long-term ocean subsurface temperature data which is not available. Thus we cannot estimate the last term of equation (5). In this section, we will focus on the net heat flux anomalies, the Ekman heat advection terms, and the anomalous entrainment heat flux term, all of which can be estimated from the long-record data of 1945–2002. The geostrophic current, calculated from satellite measurements and the Levitus climatological data, is available only after 1992. Thus its advective role on the SCS SST anomalies during the 1997–1998 El Niño will be considered as a special case study in Section 5.

4.1. First Peak of SST Anomalies

[16] Section 3 shows that the SCS interannual SST anomalies reach the first peak around February [+1] immediately following the mature phase of El Niño. Such a warming connection between the SCS and equatorial eastern Pacific is believed to be through El Niño–driven atmospheric teleconnections that alter the surface heat flux and winds that in turn change the SST in the SCS. Since we are interested in what causes the SCS SST anomalies to peak, we choose the month of November [0]—prior to the first peak as a study month. Figure 5 shows the November [0] composites of the SST anomaly tendency, net heat flux anomalies, Ekman heat advection terms, and anomalous entrainment heat flux over the SCS. In this paper, an SST anomaly tendency in a given month is calculated by the difference between the SST anomaly in the subsequent month and that in the previous one. During the boreal winter, the local atmospheric condition over the SCS is the northeast monsoon wind. When an El Niño occurs in the Pacific, the winter northeast monsoon wind over the SCS is weakened, resulting in southerly wind anomalies, as shown for the case of November [0] in Figure 6a. Thus the mean and anomalous Ekman flows in

November [0] over the SCS are northwestward and eastward, respectively. These Ekman flows, associated with the westward anomalous and southeastward mean SST gradients, induce negative value of the Ekman heat advections ($-\vec{\bar{u}}_E\nabla T' - \vec{u}'_E\nabla\bar{T} < 0$) in Figure 5c. This indicates that the Ekman heat advections cool the SCS and cannot account for the warming tendency as shown in Figure 5a. On the other hand, the weakening of the northeast monsoon wind during the winter of the El Niño year corresponds to anomalous downward Ekman pumping velocity (Figure 6a) which results in the positive entrainment heat flux anomalies in the central and southern SCS as shown in Figure 5d. However, the amplitude of the entrainment heat flux anomalies is too small to account for the SST warming.

[17] The large positive value of the net heat flux anomalies in November [0] suggests that surface heat flux is responsible for generating the first peak of the SCS SST anomalies (Figure 5b). The net surface heat flux anomalies include the components of shortwave radiation anomalies, latent heat flux anomalies, sensible heat flux anomalies, and longwave radiation anomalies. Since the amplitude of the sensible heat flux and longwave radiation anomalies in the SCS is smaller than that of the shortwave radiation and latent heat flux anomalies (not shown), we only examine the shortwave radiation and latent heat flux anomalies. We first consider the distribution of the shortwave radiation anomalies. If we linearize equation (1) of the shortwave radiation, we can get that

$$Q'_{SW} = 0.94Q_0(-0.62C'). \tag{6}$$

The shortwave radiation anomaly (Q'_{SW}) is linearly determined by the cloud cover anomaly (C'). Figure 7 shows the November [0] composites of the shortwave radiation anomalies and the cloud cover anomalies in the SCS. As expected, the pattern of the shortwave radiation anomalies is the same as that of the cloud cover anomalies, except with an opposite sign. A decrease in the cloudiness over the SCS induces an increase in the shortwave radiation.

[18] Latent heat flux is determined by wind speed and air-sea difference in specific humidity. Linearizing equation (3) results in

$$Q'_{LAT} = \rho_a L C_E\left(U'_a\Delta\bar{q} + \bar{U}_a\Delta q'\right). \tag{7}$$

The latent heat flux anomalies are attributed to variations of the wind speed anomaly (U'_a) and anomalous air-sea difference in specific humidity ($\Delta q'$). Again, equation (7) neglects the nonlinear term of $U'_a\Delta q'$ that is smaller. Figure 8 shows the November [0] composites of the latent heat flux anomalies and the contributions of the wind speed anomaly and of anomalous air-sea difference in specific humidity to the latent heat flux anomalies. During the winter of the El Niño year, the northeast monsoon wind

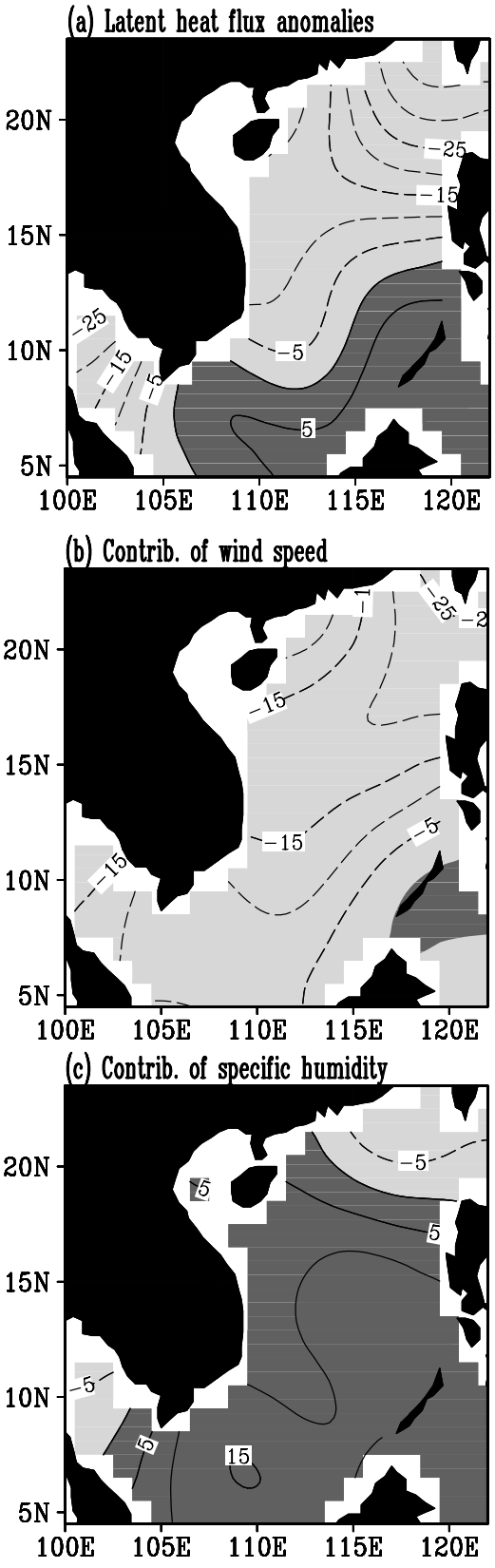

Figure 8. November [0] composites of (a) the latent heat flux anomalies, (b) the contribution of the wind speed anomaly to the latent heat flux anomalies, and (c) the contribution of anomalous air-sea difference in specific humidity to the latent heat flux anomalies. Positive latent heat flux indicates that the ocean gives heat to the atmosphere. Units are W/m^2. Positive (negative) values are given by dark (light) shading and solid (dashed) contour lines.

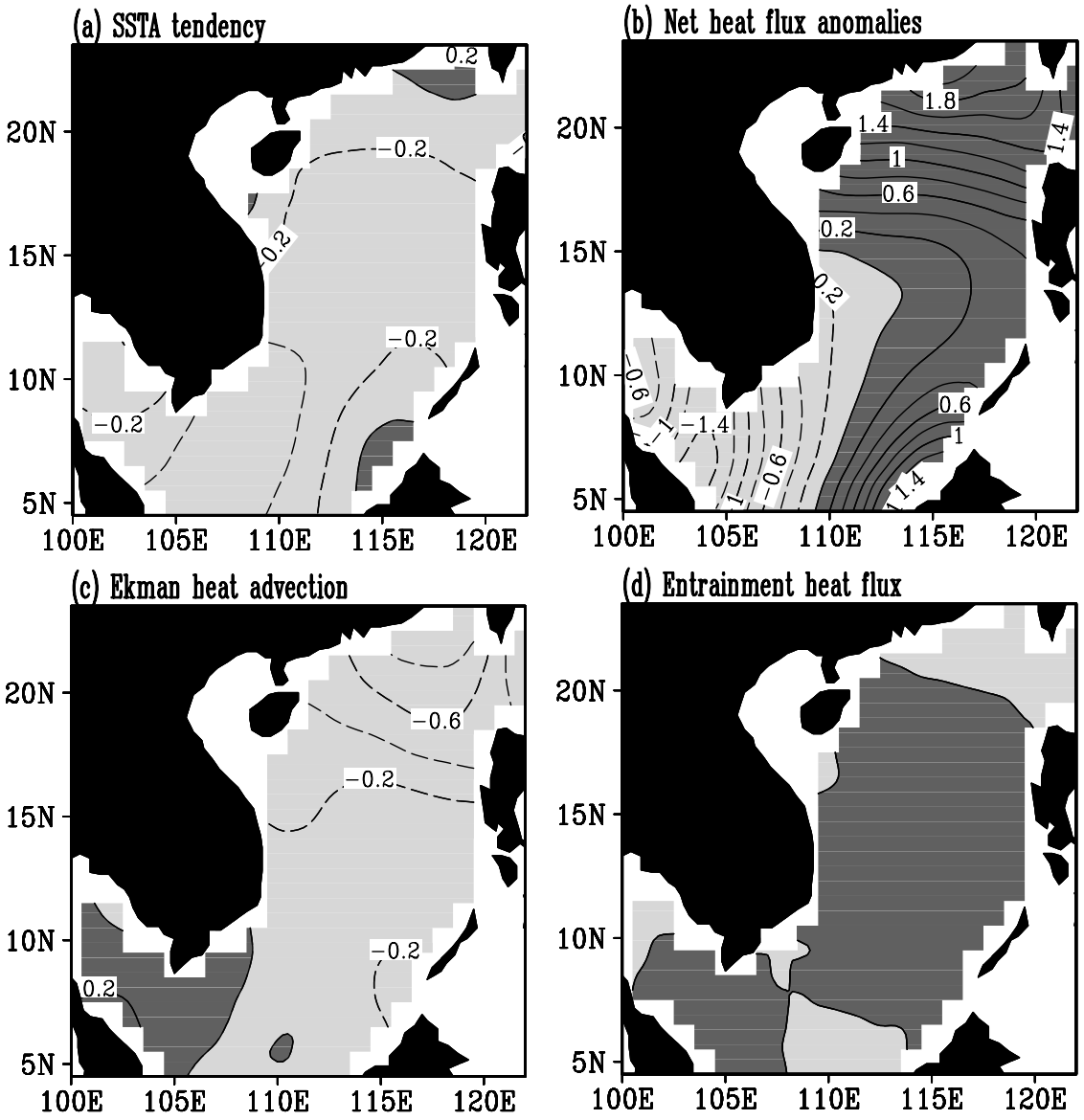

Figure 9. April [+1] composites of (a) the SST anomaly tendency, (b) net heat flux anomalies ($Q'_{NET}/\rho C_P \bar{h}$), (c) Ekman heat advections ($-\vec{u}_E \nabla T' - \vec{u}'_E \nabla \bar{T}$), and (d) anomalous entrainment heat flux ($-w'_E \partial \bar{T}/\partial z$). Positive (negative) values are given by dark (light) shading and solid (dashed) contour lines, and contour interval is 0.2°C per 2 months.

over the SCS is weakened, with maximum weakening occurring in the northern SCS (Figure 6a). The weakening of the northeast monsoon decreases the wind speed that results in negative heat flux anomalies centered in the northern SCS (Figure 8b). On the other hand, the contribution of anomalous air-sea difference in specific humidity to the latent heat flux anomalies is positive over the southern and central SCS (Figure 8c). The combined effect is negative (positive) latent heat flux anomalies in the northern (southern) SCS (Figure 8a). Note that positive latent heat flux is defined as heat loss from the ocean. In summary, the positive net heat flux anomalies in November [0], which are responsible for the SCS warming, mainly result from increase in the shortwave radiation anomalies (attributed to cloudiness anomalies) and decrease in the latent heat flux anomalies (attributed to both the wind speed anomalies and anomalous air-sea difference in specific humidity).

4.2. Decay of SST Anomalies Following the First Peak

[19] The last section shows that when El Niño in the Pacific matures during the winter, it induces changes of cloud cover, wind, and humidity in the SCS that in turn warm the SCS up mainly through the surface heat flux anomalies. After reaching the peak in February [+1], the SCS SST anomalies then decay. What are physical processes that are responsible for the decay of the SCS SST anomalies after February [+1]? We choose the month of April [+1] for studying the decay of the SCS SST anomalies. Figure 9 shows the April [+1] composites of the SST anomaly tendency, net heat flux anomalies, Ekman heat advections, and anomalous entrainment heat flux.

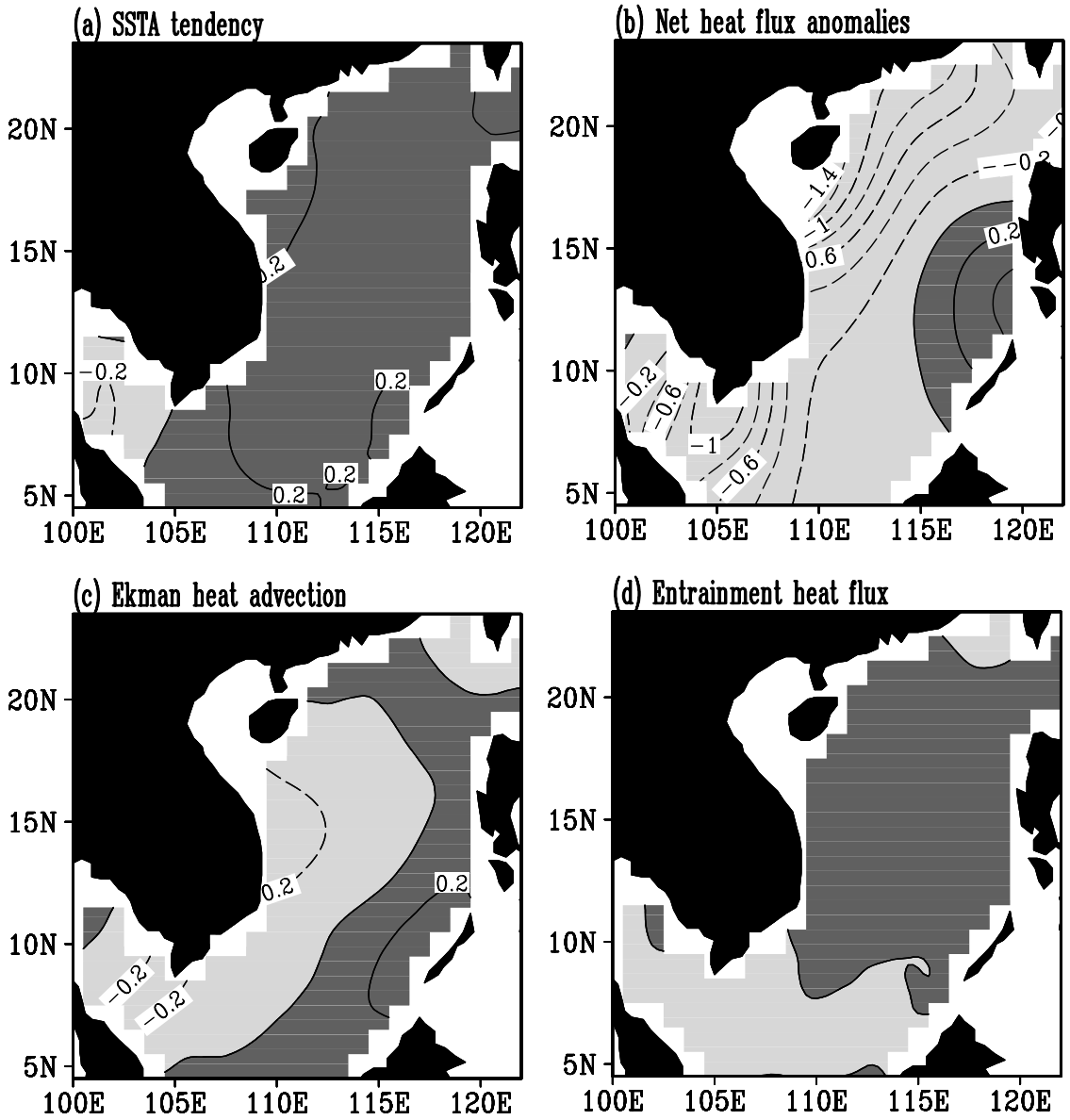

Figure 10. July [+1] composites of (a) the SST anomaly tendency, (b) net heat flux anomalies ($Q'_{NET}/\rho C_P \bar{h}$), (c) Ekman heat advection ($-\vec{\bar{u}}_E \nabla T' - \vec{u}'_E \nabla \bar{T}$), and (d) anomalous entrainment heat flux ($-w'_E \partial \bar{T}/\partial z$). Positive (negative) values are given by dark (light) shading and solid (dashed) contour lines, and contour interval is 0.2°C per 2 months.

Over most regions of the SCS the net heat flux anomalies are positive, except for the region of the Sunda shelf and the South Vietnam coast (Figure 9b). Comparison of Figure 5b and Figure 9b shows that the net heat flux anomalies in the central and southwestern SCS are reduced, favoring the decay of SST anomalies. In April [+1], the SCS is still associated with a weakening of the northeast monsoon with strong southerly wind anomalies in the central and northern SCS (Figure 6b). Correspondingly, the wind pattern produces an anomalous downward Ekman pumping velocity (Figure 6b) that results in positive anomalous entrainment heat flux (Figure 9d). Thus the anomalous entrainment heat flux during that time tends to warm the SCS (in spite of a small amplitude).

[20] However, the mean and anomalous Ekman heat advections tend to cool the SCS (Figure 9c). The wind patterns over the SCS in the subsequent spring of the El Niño year are similar to those in the winter of the El Niño year. Similar to the case of November [0], both the mean northwestward and anomalous eastward Ekman flows (associated with the mean northeast monsoon and anomalous southerly winds, respectively) in April [+1] contribute to the negative value of the Ekman heat advections shown in Figure 9c. The negative Ekman heat advections, assisted with the reduction of the surface heat flux anomalies, cool the SCS in April [+1].

4.3. Second Peak of SST Anomalies

[21] Since the second peak of the SCS SST anomalies occurs in August [+1], we choose the month of July [+1] for evaluating roles of various processes in the second peak. Figure 10 shows the July [+1] composites

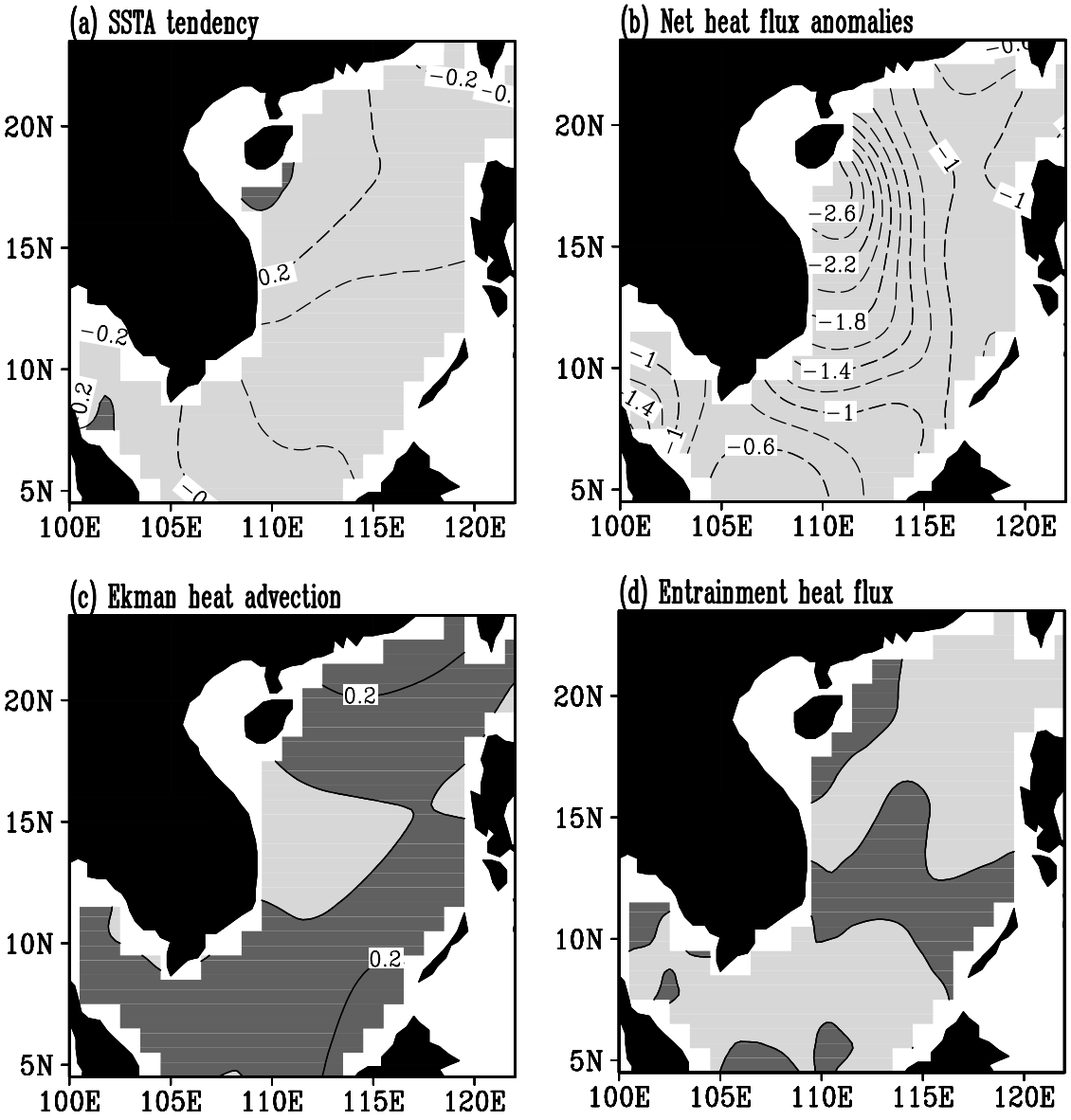

Figure 11. September [+1] composites of (a) the SST anomaly tendency, (b) net heat flux anomalies ($Q'_{NET}/\rho C_P \bar{h}$), (c) Ekman heat advection ($-\vec{\bar{u}}_E \nabla T' - \vec{u}'_E \nabla \bar{T}$), and (d) anomalous entrainment heat flux ($-w'_E \partial \bar{T}/\partial z$). Positive (negative) values are given by dark (light) shading and solid (dashed) contour lines, and contour interval is 0.2°C per 2 months.

of the SST anomaly tendency, net heat flux anomalies, Ekman heat advection terms, and anomalous entrainment heat flux. The net heat flux anomalies are negative almost everywhere in the SCS (Figure 10b). The Ekman heat advections are also negative over the western and central SCS (Figure 10c). The only process in Figure 10 that can warm the SCS is the positive anomalous entrainment heat flux (Figure 10d) that results from a downward anomalous Ekman pumping velocity in July [+1] (Figure 6c). However, the amplitude of the positive anomalous entrainment heat flux is too small to account for the warming of the second peak. This means that other processes must be responsible for the warming of the second peak. Section 5 will show that during the 1997–1998 El Niño the geostrophic heat advection is important for the second SST anomaly peak occurring in August of 1998.

4.4. Decay of SST Anomalies Following the Second Peak

[22] After the second peak in August [+1], the SCS SST anomalies decay again. Figure 11 shows the September [+1] composites of the SST anomaly tendency, net heat flux anomalies, Ekman heat advection terms, and anomalous entrainment heat flux. September is a transition month for the SCS monsoon to switch from the summer southwest monsoon wind to the winter northeast monsoon wind. The wind anomalies over the SCS in September [+1] are weakly northeasterly, as shown in Figure 6d. Correspondingly, both the Ekman advections and anomalous entrainment heat flux

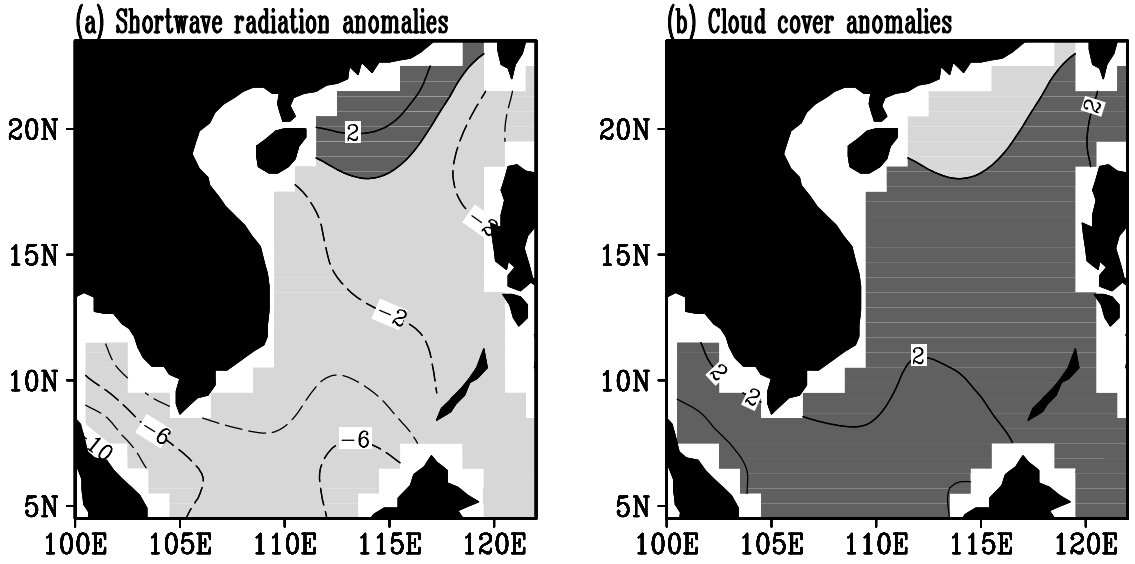

Figure 12. September [+1] composites of (a) the shortwave radiation anomalies (W/m^2) and (b) the cloud cover anomalies (%) in the SCS. Positive (negative) values are given by dark (light) shading and solid (dashed) contour lines.

are small (Figures 11c and 11d), suggesting that they cannot cool the SCS. The large negative value of the net heat flux anomalies (Figure 11b) indicates that the surface heat flux anomalies are responsible for the negative SST anomaly tendency in September [+1].

[23] Again, we only examine the shortwave radiation and latent heat flux anomalies due to the smallness of the sensible heat and longwave radiation anomalies. Figures 12 and 13 show the September [+1] composites of the shortwave radiation and latent heat flux anomalies, respectively. The shortwave radiation anomalies show a small negative value over the southern SCS that is induced by increase of cloudiness (Figures 12a and 12b). Comparison of Figures 13a, 13b, and 13c shows that the contribution of the wind speed anomalies to the latent heat flux anomalies is smaller than that of the anomalous air-sea difference in specific humidity. That is, the latent heat flux anomalies in September [+1] are largely determined by the anomalous air-sea difference in specific humidity. The small contribution of the wind speed anomalies to the latent heat flux anomalies is consistent with that the wind anomalies are weak in September [+1] (Figure 6d). In summary, the cooling of the SCS after the second peak is mainly due to the increase of the latent heat flux anomalies that result largely from the increase in the anomalous air-sea difference in specific humidity.

5. Case Study of Geostrophic Advections: The 1997–1998 El Niño

[24] There is no direct measurement of geostrophic current in the SCS. To estimate its advective role in the SST anomalies, we have to calculate geostrophic current from observational data. Satellite measurement of the SSH provides us a possible way to calculate the geostrophic current in the SCS. Satellite altimeters observe only temporal deviations from the long-term mean SSH. Thus we add the annual mean geostrophic current estimated from the Levitus data to that calculated from the SSH data. A 3-month running mean is applied to the geostrophic current anomalies. Since the SSH data is only available after 1992, we consider the 1997–1998 El Niño as a case study for evaluating the role of geostrophic advections in the SCS SST anomalies.

[25] The estimated geostrophic currents in the SCS during the boreal winter and summer are shown in Figures 14a and 14b, respectively. In the winter (January), when the northeast monsoon wind prevails over the SCS, the geostrophic current shows a basin-wide cyclonic circulation (Figure 14a). In the summer (July), because of the southwest monsoon most of ocean flows in the SCS are northeastward with a strong geostrophic flow in the east of the Vietnam coast (Figure 14b). This geostrophic flow pattern is consistent with previous estimations [e.g., *Qu*, 2001; *Yang et al.*, 2002; *Liu et al.*, 2004], giving us confidence in our calculations.

[26] With the estimated geostrophic current in the SCS, we can compute the geostrophic advection terms in equation (5). Figure 15 shows the SST anomaly tendency, sum of geostrophic advection terms, mean zonal geostrophic advection ($-\bar{u}_G \partial T'/\partial x$), anomalous zonal geostrophic advection ($-u'_G \partial \bar{T}/\partial x$), mean meridional geostrophic advection ($-\bar{v}_G \partial T'/\partial y$), and the anomalous meridional geostrophic advection ($-v'_G \partial \bar{T}/\partial y$) in November of 1997. The net effect of four geostrophic advection terms shows a cooling over most regions of the SCS, except for the region of the narrow western boundary (Figure 15b). The contributions of individual terms largely manifest the distributions of anomalous and mean geostrophic flows in November of 1997. In response to the winter northeast monsoon wind, the November climatological geostrophic flows are northeastward in the eastern/central SCS and southwestward in the narrow western boundary region (not shown). This mean geostrophic flow pattern results in a negative (positive) value of $-\bar{u}_G \partial T'/\partial x$ ($-\bar{v}_G \partial T'/\partial y$) over most areas of the SCS (Figures 15c and 15e). The anomalous geostrophic flow in the SCS during November of 1997

displays an anticyclonic circulation, with a southwestward (northeastward) flow in the eastern (western) SCS (not shown). Thus the anomalous geostrophic flow induces a positive (negative) value of $-u'_G\partial\bar{T}/\partial x$ in the southeastern (northwestern) SCS (Figure 15d) and a negative (positive) value of $-v'_G\partial\bar{T}/\partial y$ in the southeastern (northwestern) SCS (Figure 15f).

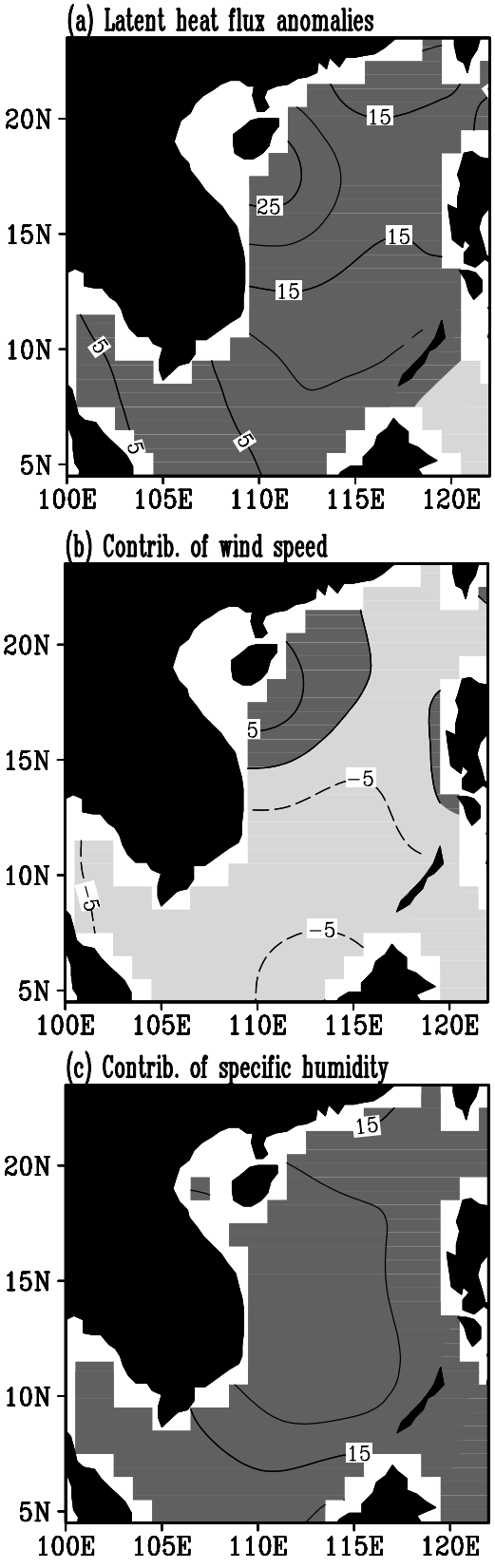

[27] After reaching the peak in February of 1998, the SCS SST anomalies decay. The SST anomaly tendency and the roles of the geostrophic heat advections for the decay in April of 1998 are shown in Figure 16. The geostrophic heat advections cool the western SCS as shown in Figure 16b. The cooling of the geostrophic advections is mainly attributed to the mean meridional advection and anomalous meridional advection (Figures 16e and 16f). In April of 1998, the mean (anomalous) geostrophic current is northeastward (southwestward) over the central/western SCS (not shown). These flows, associated with the positive (negative) anomalous (mean) meridional SST gradients, result in cooling effect of $-\bar{v}_G\partial T'/\partial y$ and $-v'_G\partial\bar{T}/\partial y$ as shown in Figures 16e and 16f. Figure 16c shows that the contribution of the mean zonal geostrophic advection in the western SCS is a warming effect.

[28] The SCS SST anomalies peak again in August of 1998. The SST anomaly tendency and geostrophic advection terms in July of 1998 (just before the peak) are shown in Figure 17. The net effect of the geostrophic advections is a warming in the central and northeastern SCS, and a cooling in the southern SCS (Figure 17b). The major contribution of the warming is the mean meridional geostrophic advection (Figure 17e). This is because the climatological mean geostrophic flow in July is northeastward (Figure 14b) that induces a warming tendency of $-\bar{v}_G\partial T'/\partial y$ associated with a negative value of anomalous meridional SST gradient.

[29] After the second peak in August of 1998, the SCS SST anomalies decay again. Figure 18 shows the SST anomaly tendency and geostrophic advection terms in September of 1998. The cooling of the geostrophic advections occurs in the southern SCS (Figure 18b). The cooling is due to the mean zonal geostrophic advection (Figure 18c). The climatological mean geostrophic flow in September is northeastward over the southern SCS (not shown). The mean northeastward flow, associated with a positive anomalous zonal SST gradient, results in the cooling effect of $-\bar{u}_G\partial T'/\partial x$ over the southern SCS as shown in Figure 18c.

[30] As the 1997–1998 El Niño occurs in the Pacific, the SCS SST anomalies evolve with two peak and two decay phases. It is worthy to compare the roles of geostrophic advections in these two peak (and decay) phases. Comparison of Figures 15 and 17 shows that the roles of the mean zonal and meridional geostrophic advections are approximately similar for the first and second peaks of the SST anomalies. However, the patterns of the anomalous meridional geostrophic advection for the first and second peaks

Figure 13. September [+1] composites of (a) the latent heat flux anomalies, (b) the contribution of the wind speed anomaly to the latent heat flux anomalies, and (c) the contribution of anomalous air-sea difference in specific humidity to the latent heat flux anomalies. Positive latent heat flux indicates that the ocean gives heat to the atmosphere. Units are W/m^2. Positive (negative) values are given by dark (light) shading and solid (dashed) contour lines.

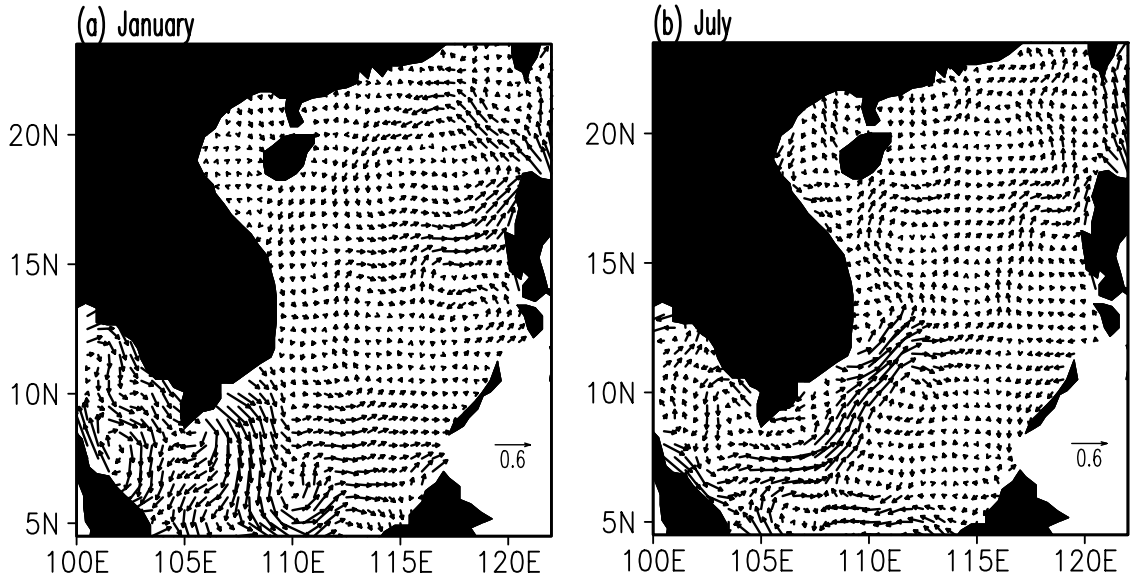

Figure 14. Geostrophic currents (m/s) in the South China Sea (SCS) during (a) winter (January) and (b) summer (July). The currents are calculated from the satellite measurement of sea surface height data and the Levitus climatological data.

are opposite. The anomalous meridional geostrophic advection in November of 1997 shows a negative (positive) value in the eastern (western) part of the SCS, whereas it is positive (negative) in the eastern (western) SCS in July of 1998. For two decay phases, various advection terms play a different role. In April of 1998, the mean and anomalous meridional geostrophic advections cool SST, whereas the mean zonal geostrophic advection plays a warming effect over the western SCS. During the second decay phase of September of 1998, the contribution of the mean zonal geostrophic advection is a cooling effect.

6. Summary and Discussion

[31] ENSO affects the global ocean through atmospheric bridges or teleconnections. The South China Sea (SCS) is embedded between the western Pacific Ocean and the eastern Indian Ocean. Its variations are, of course, influenced by ENSO events [e.g., *Klein et al.*, 1999; *Alexander et al.*, 2002; *D. Wang et al.*, 2002; *Liu et al.*, 2004]. The present paper discovers that the interannual SST anomalies over the SCS show a double-peak feature following El Niño event in the Pacific. The first and second peaks occur around February [+1] and August [+1], respectively in the subsequent year of the El Niño year. Observational data show that the net heat flux anomaly is a major contribution to the first peak of the SCS SST anomalies although the geostrophic heat advections warm the western boundary region. After the first peak of February [+1], both the Ekman and geostrophic heat advections act to cool the SCS. In August [+1], the mean meridional geostrophic heat advection makes the SCS SST anomalies peak again. Then, the net heat flux anomalies and the mean zonal geostrophic heat advection take over for the cooling of the SCS after the second peak.

[32] The linkage between El Niño and the SCS is believed to be through the atmospheric bridge of atmospheric circulation changes. During El Niño, the regional Hadley circulation in the Indo-western Pacific sector is weakened, with anomalous decent over the tropical Indo-western Pacific [*Klein et al.*, 1999; *Wang*, 2002, 2005]. Corresponded to the anomalous decent are anomalous anticyclones in the off-equatorial western Pacific during and after the mature phase of El Niño [e.g., *Weisberg and Wang*, 1997; *Wang et al.*, 1999]. The anomalous anticyclone in the north western Pacific, associated with the anomalous decent motion, alters the local SCS near-surface air temperature, humidity, and monsoon wind, as well as the distribution of clouds. These changes influence surface heat fluxes and oceanic circulation that in turn induce the SST variations over the SCS.

[33] When El Niño in the Pacific matures in the boreal winter, the SCS shows anomalous decent motion and weakening of the winter northeast monsoon in response to the anomalous anticyclone in the north western Pacific. These decrease the cloudiness over the SCS that increases the shortwave radiation anomalies and warms the SCS SST. The El Niño–driven atmospheric conditions in the SCS also decrease the wind speed and change air-sea difference in specific humidity. Both the wind speed anomalies and anomalous air-sea difference in specific humidity contribute to the latent heat flux anomalies that play a role for the first peak of the SCS SST anomalies in February [+1]. In addition, the mean and anomalous meridional geostrophic currents show a warming effect over the western boundary region of the SCS.

[34] After the first peak in February [+1], the net surface heat flux anomalies are reduced over the SCS. The El Niño–driven weakening of the northeast monsoon wind is also continued over the SCS during the subsequent spring of the El Niño year. Thus, in April [+1], the mean Ekman velocity is northwestward and the anomalous Ekman velocity is southeastward. These Ekman flows, combined with a northwestward (southwestward) anomalous (mean) SST

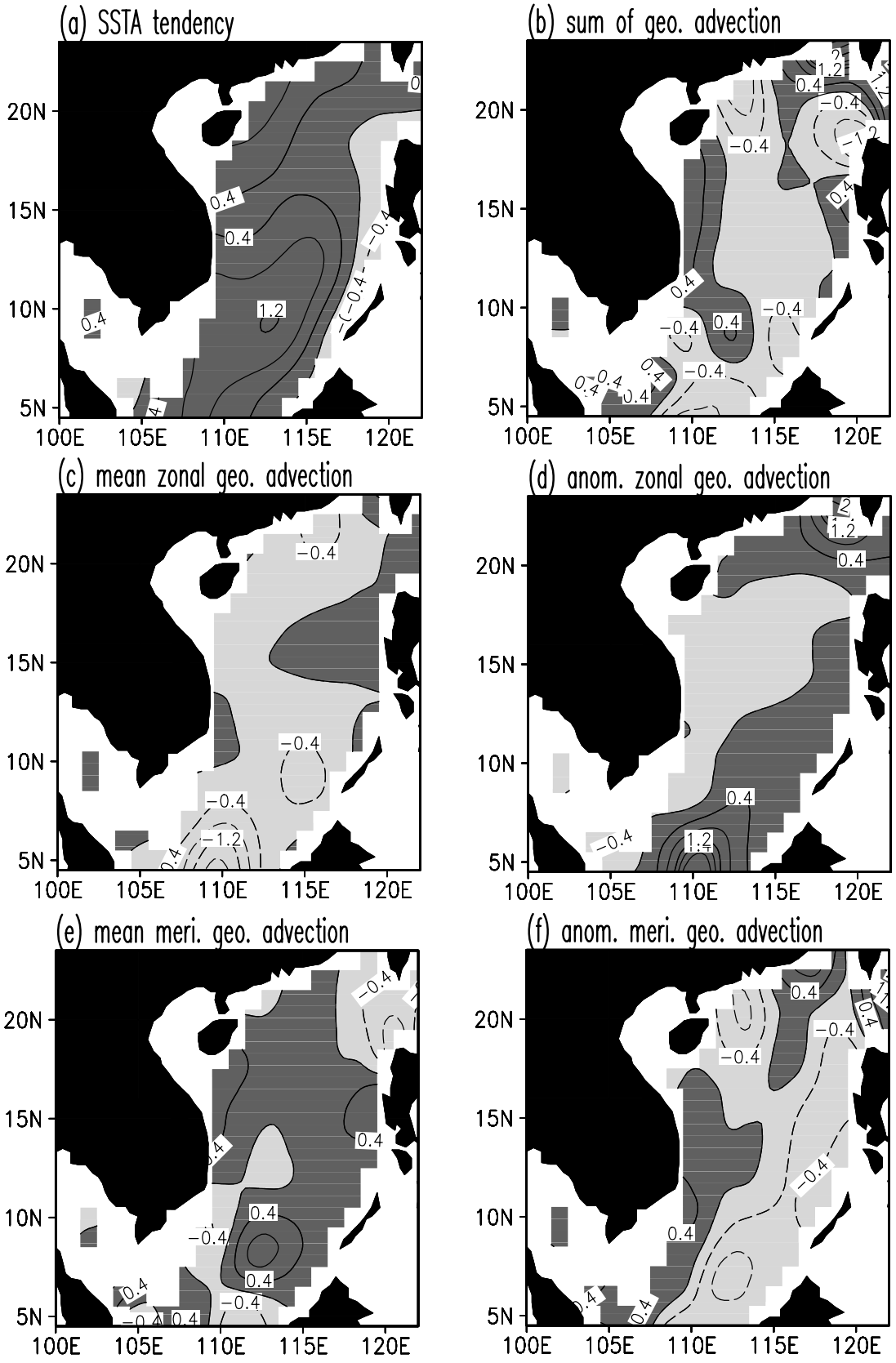

Figure 15. (a) SST anomaly tendency, (b) sum of geostrophic advections, (c) mean zonal geostrophic advection ($-\bar{u}_G \partial T'/\partial x$), (d) anomalous zonal geostrophic advection ($-u'_G \partial \bar{T}/\partial x$), (e) mean meridional geostrophic advection ($-\bar{v}_G \partial T'/\partial y$), and (f) anomalous meridional geostrophic advection ($-v'_G \partial \bar{T}/\partial y$) in November of 1997. Positive (negative) values are given by dark (light) shading and solid (dashed) contour lines, and contour interval is 0.4°C per 2 months.

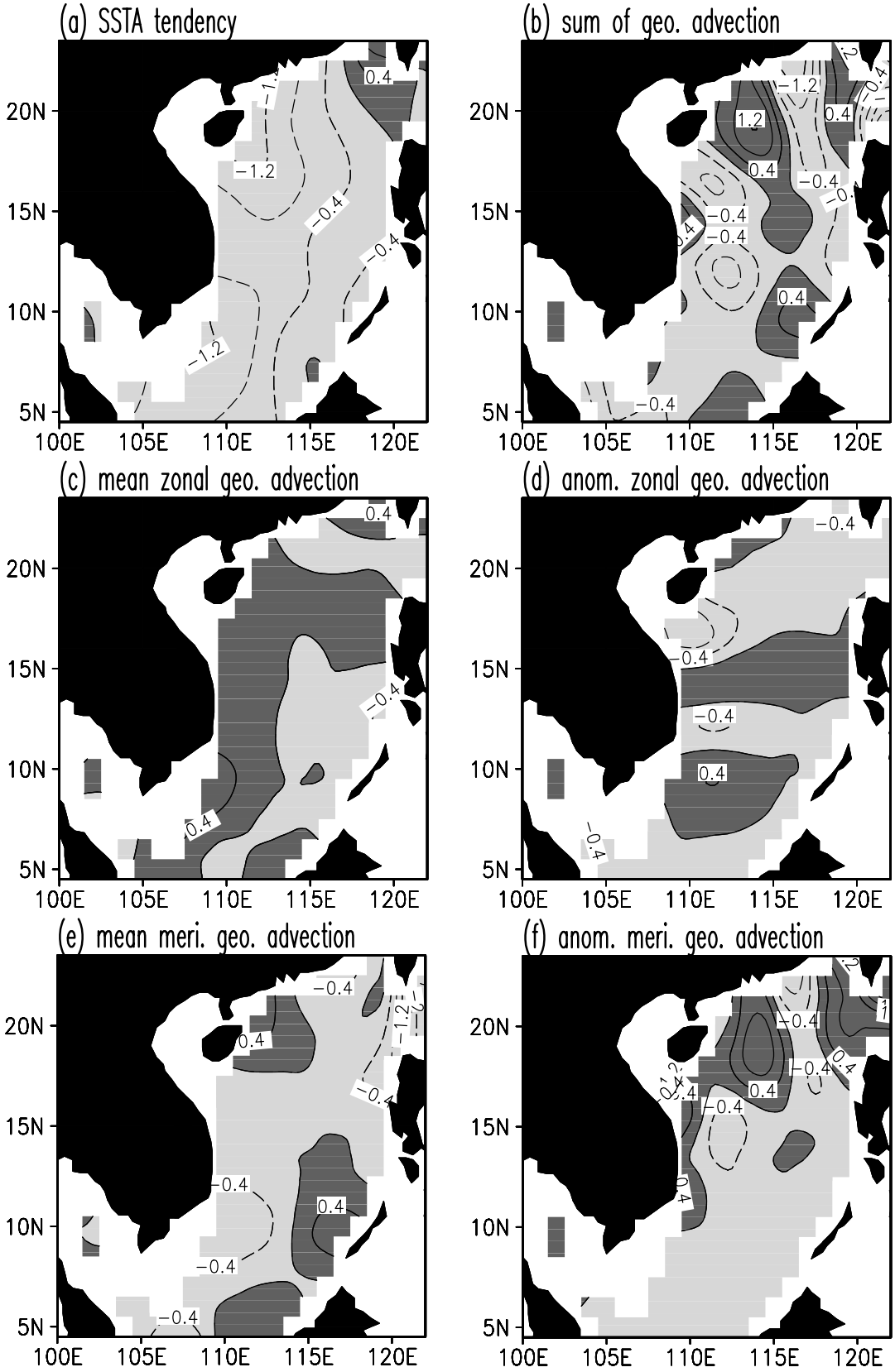

Figure 16. (a) SST anomaly tendency, (b) sum of geostrophic advections, (c) mean zonal geostrophic advection ($-\bar{u}_G \partial T'/\partial x$), (d) anomalous zonal geostrophic advection ($-u'_G \partial \bar{T}/\partial x$), (e) mean meridional geostrophic advection ($-\bar{v}_G \partial T'/\partial y$), and (f) anomalous meridional geostrophic advection ($-v'_G \partial \bar{T}/\partial y$) in April of 1998. Positive (negative) values are given by dark (light) shading and solid (dashed) contour lines, and contour interval is 0.4°C per 2 months.

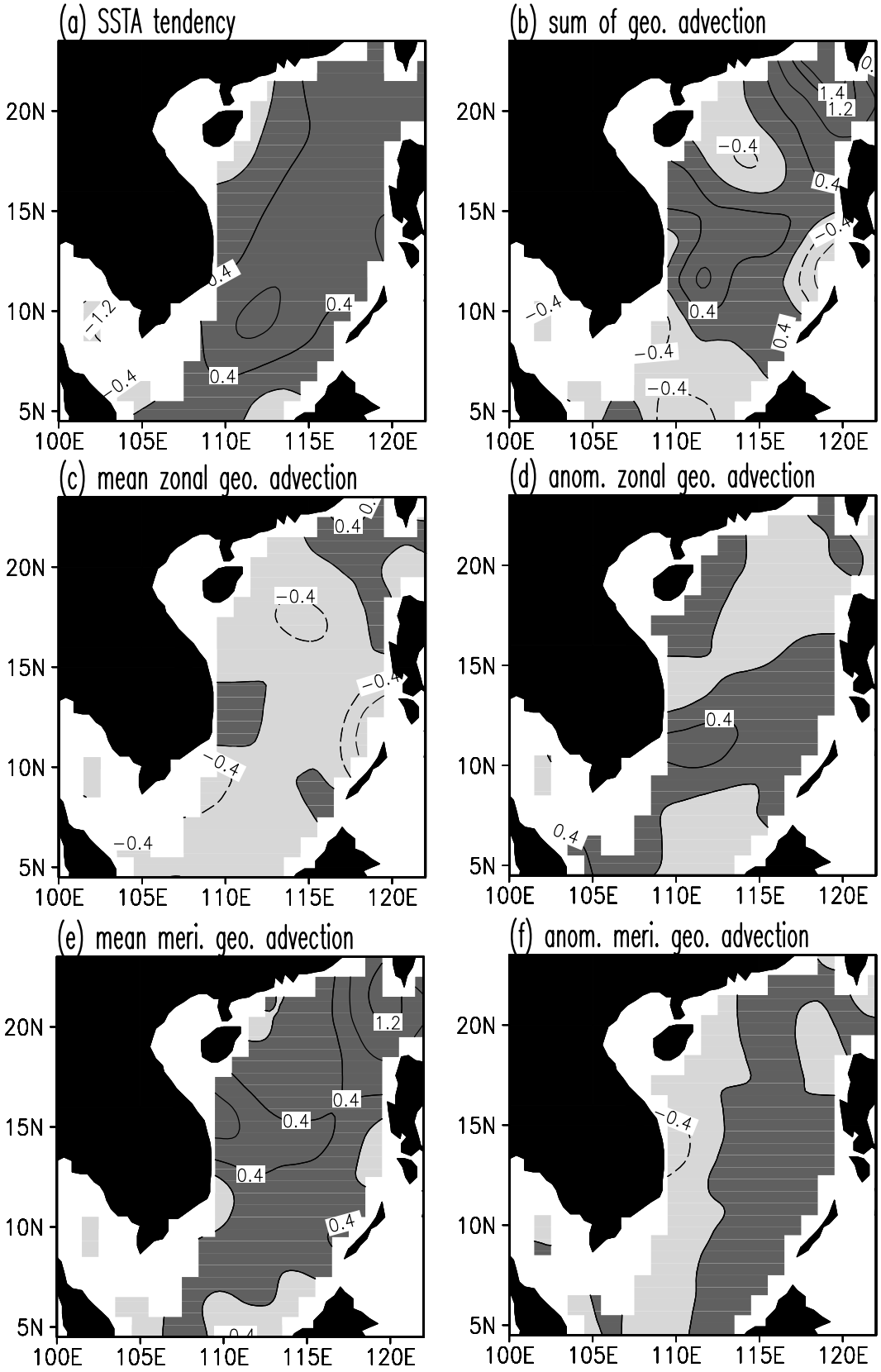

Figure 17. (a) SST anomaly tendency, (b) sum of geostrophic advections, (c) mean zonal geostrophic advection ($-\bar{u}_G \partial T'/\partial x$), (d) anomalous zonal geostrophic advection ($-u'_G \partial \bar{T}/\partial x$), (e) mean meridional geostrophic advection ($-\bar{v}_G \partial T'/\partial y$), and (f) anomalous meridional geostrophic advection ($-v'_G \partial \bar{T}/\partial y$) in July of 1998. Positive (negative) values are given by dark (light) shading and solid (dashed) contour lines, and contour interval is 0.4°C per 2 months.

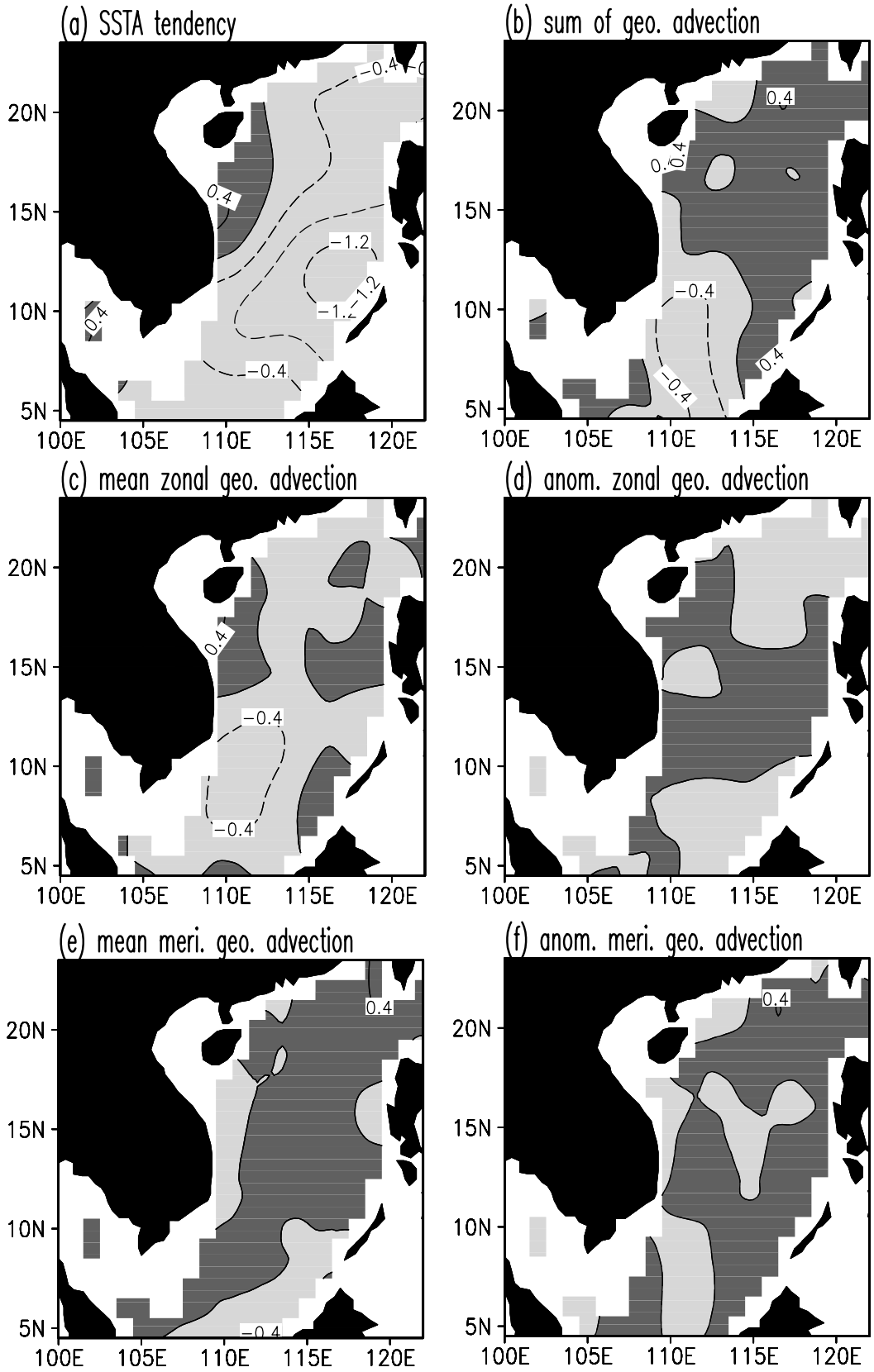

Figure 18. (a) SST anomaly tendency, (b) sum of geostrophic advections, (c) mean zonal geostrophic advection ($-\bar{u}_G \partial T'/\partial x$), (d) anomalous zonal geostrophic advection ($-u'_G \partial \bar{T}/\partial x$), (e) mean meridional geostrophic advection ($-\bar{v}_G \partial T'/\partial y$), and (f) anomalous meridional geostrophic advection ($-v'_G \partial \bar{T}/\partial y$) in September of 1998. Positive (negative) values are given by dark (light) shading and solid (dashed) contour lines, and contour interval is 0.4°C per 2 months.

gradient, produce a cooling effect for the SCS as shown in Figure 9d. During April [+1] the mean and anomalous geostrophic currents over the SCS are northeastward and southwestward, respectively. These geostrophic currents also help cool the SCS after the first peak of SST anomalies.

[35] The SCS SST anomalies peak again in August [+1] and then decay. The negative values of the surface heat flux and Ekman heat advections and the smallness of anomalous entrainment heat flux cannot explain the second peak of the SCS SST anomalies. Our analyses show that the mean meridional geostrophic heat advection is mainly responsible for the second peak. The mean geostrophic current of the SCS in the summer is northeastward in response to the southwest monsoon. The mean northward current, associated with a southward anomalous SST gradient, results in a warming condition in the SCS as shown in Figure 17e. After the second peak, the latent heat flux anomalies, mainly attributed to the anomalous air-sea difference in specific humidity, cool the SCS. It is worth to note that the mean northeastward geostrophic current also helps cool the southern SCS in September [+1].

[36] The anomalous entrainment heat flux is always positive over various stages of the SCS SST anomaly evolution. This occurs because the anomalous Ekman pumping velocity over the SCS is always downward following El Niño events (Figure 6). The downward anomalous Ekman pumping and the positive mean vertical temperature gradient produce a warming trend in the SCS. However, the amplitude of the anomalous entrainment heat flux is smaller than other terms in the SST equation, and thus it plays a secondary role in the SCS SST anomalies.

[37] This paper mainly focuses on the SCS SST anomalies associated with the warm phase (El Niño) of ENSO. A natural question to be asked is: How do the SCS SST anomalies vary during the cold phase (La Niña) of ENSO? Our analyses show that the double-peak evolution of the SCS SST anomalies following La Niña events in the Pacific is not a common feature. Only in the 1964–1965 and 1975–1976 La Niña events does the SCS show two cold peaks of the SST anomalies (two peaks occur in the winter of the La Niña year and the subsequent spring of the La Niña year, respectively). For some La Niña events, the SCS does not even show cold SST anomalies. These imply that the response of the SCS SST anomalies to El Niño and La Niña is not symmetric. However, for the cases that the SCS does show cold SST anomalies following La Niña events, the net surface heat flux anomalies play a major role. Finally, we would like to caution that the heat budget calculations in this paper are based on multiple observational data sets described in Section 2, and thus the roles of various terms in the SCS SST anomalies may depend upon these data sets. Nevertheless, these data sets are probably the best long-term data available for us to study interannual variability over the SCS.

[38] **Acknowledgments.** We thank S.-P. Xie and T. Qu for discussions during the early stage of the work. Comments by reviewers and the editor are appreciated. The work was done when W.W. and D.W. visited the National Oceanic and Atmospheric Administration (NOAA) Atlantic Oceanographic and Meteorological Laboratory (AOML). This work is supported by a grant from NOAA Office of Global Programs, the base funding of NOAA/AOML, National Natural Science Foundation of China (grants 40476009, 40306003, and 40136010), National Basic Research Program of China (grant 2005CB422301), and the funding of the K. C. Wong Education Foundation. The findings and conclusions in this report are those of the author(s) and do not necessarily represent the views of the funding agency.

References

Alexander, M. A., et al. (2002), The atmospheric bridge: The influence of ENSO teleconnections on air-sea interaction over the global oceans, *J. Clim.*, *15*, 2205–2231.

da Silva, A., C. Young-Molling, and S. Levitus (1994), *Atlas of Surface Marine Data 1994*, vol. 3, *Anomalies of Heat and Momentum Fluxes*, *NOAA Atlas NESDIS*, vol. 8, NOAA, Silver Spring, Md.

Ducet, N., P. Y. Le Traon, and G. Reverdin (2000), Global high-resolution mapping of ocean circulation from TOPEX/Poseidon and WRS-1 and -2, *J. Geophys. Res.*, *105*, 19,477–19,498.

Fung, I. Y., D. E. Harrison, and A. A. Lacis (1984), On the variability of the net longwave radiation at the ocean surface, *Rev. Geophys.*, *22*, 177–193.

Klein, S. A., B. J. Soden, and N. C. Lau (1999), Remote sea surface temperature variations during ENSO: Evidence for a tropical Atmospheric bridge, *J. Clim.*, *12*, 917–932.

Levitus, S., and T. P. Boyer (1994), *World Ocean Atlas 1994*, vol. 4, *Temperature, NOAA Atlas NESDIS*, vol. 4, 129 pp., NOAA, Silver Spring, Md.

Liu, Q., X. Jiang, S.-P. Xie, and W. T. Liu (2004), A gap in the Indo-Pacific warm pool over the South China Sea in boreal winter: Seasonal development and interannual variability, *J. Geophys. Res.*, *109*, C07012, doi:10.1029/2003JC002179.

Qu, T. (2001), Role of ocean dynamics in determining the mean seasonal cycle of the South China Sea surface temperature, *J. Geophys. Res.*, *106*, 6943–6955.

Qu, T., et al. (2004), Can Luzon strait transport play a role in conveying the impact of ENSO to the South China Sea?, *J. Clim.*, *17*, 3644–3657.

Wang, C. (2002), Atmospheric circulation cells associated with the El Niño–Southern Oscillation, *J. Clim.*, *15*, 399–419.

Wang, C. (2005), ENSO, Atlantic climate variability, and the Walker and Hadley circulations, in *The Hadley Circulation: Past, Present and Future*, edited by H. F. Diaz and R. S. Bradley, pp. 173–202, Springer, New York.

Wang, C., R. H. Weisberg, and J. I. Virmani (1999), Western Pacific interannual variability associated with the El Niño–Southern Oscillation, *J. Geophys. Res.*, *104*, 5131–5149.

Wang, C., S.-P. Xie, and J. A. Carton (2004), A global survey of ocean-atmosphere interaction and climate variability, in *Earth's Climate: The Ocean-Atmosphere Interaction*, *Geophys. Monogr. Ser.*, vol. 147, edited by C. Wang, et al., pp. 1–19, AGU, Washington, D. C.

Wang, D., Q. Xie, Y. Du, W. Q. Wang, and J. Chen (2002), The 1997–1998 warm event in the South China Sea, *Chin. Sci. Bull.*, *47*, 1221–1227.

Wang, Q., Q. Liu, R. Hu, and Q. Xie (2002), A possible role of the South China Sea in ENSO cycle, *Acta Oceanol. Sin.*, *21*, 217–226.

Wang, W., D. Wang, and Y. Qi (2000), Large-scale characteristics of interannual variability of sea surface temperature in the South China Sea, *Acta Oceanol. Sin.*, *22*, 8–16.

Weisberg, R. H., and C. Wang (1997), A western Pacific oscillator paradigm for the El Niño–Southern Oscillation, *Geophys. Res. Lett.*, *24*, 779–782.

Woodruff, S. D., R. J. Slutz, R. L. Jenne, and P. M. Steurer (1987), A comprehensive ocean-atmosphere data set, *Bull. Am. Meteorol. Soc.*, *68*, 521–527.

Xie, S.-P., Q. Xie, D. Wang, and W. T. Liu (2003), Summer upwelling in the South China Sea and its role in regional climate variations, *J. Geophys. Res.*, *108*(C8), 3261, doi:10.1029/2003JC001867.

Yang, H., Q. Liu, Z. Liu, D. Wang, and X. Liu (2002), A general circulation model study of the dynamics of the upper ocean circulation of the South China Sea, *J. Geophys. Res.*, *107*(C7), 3085, doi:10.1029/2001JC001084.

C. Wang, Atlantic Oceanographic and Meteorological Laboratory, Physical Oceanography Division, NOAA, 4301 Rickenbacker Causeway, Miami, FL 33149, USA. (chunzai.wang@noaa.gov)

D. Wang and W. Wang, Key Laboratory of Tropical Marine Environmental Dynamics, South China Sea Institute of Oceanology, Chinese Academy of Sciences, 164 West Xingang Rd., Guangzhou 510301, China.

Q. Wang, Department of Meteorology, Physical Oceanography Laboratory, Ocean University of China, 5 Yushan Road, Qingdao 266003 China.